Volume 14, Issue 4, 142436 (1-17)

Iranian Journal of Catalysis (IJC)

https://doi.org/10.57647/j.ijc.2024.1404.36

Facile synthesis of waste tire scrap derived activated carbon-ZnO nanocomposite for the photodegradation of malachite green and antibacterial activity

Syed Nizam Uddin Shah Bukhari[1,2], Aqeel Ahmed Shah[3,*], Muhammad Ali Bhatti[4], Wen Liu[1,*], Abdul Karim Shah[5], Zaffar Hussain Ibhupoto[6], Anjum Zehra Naqvi[7]

[1]*State Key Laboratory of Chemical Resource Engineering, Beijing Advanced Innovation Center for Soft Matter Science and Engineering, College of Chemistry, Beijing University of Chemical Technology, China.*
[2]*Department of Basic Science and Humanities, Dawood University of Engineering and Technology, Karachi, Pakistan.*
[3]*Wet Chemistry Laboratory, Department of Metallurgical Engineering, NED University of Engineering and Technology, University Road, Karachi, Pakistan.*
[4]*Department of Environmental Sciences, University of Sindh Jamshoro, Pakistan.*
[5]*Department of Chemical Engineering, Dawood University of Engineering and Technology, Karachi, Sindh, Pakistan.*
[6]*University of Sindh, Jamshoro, Pakistan.*
[7]*Department of Microbiology, University of Karachi, Karachi, Pakistan.*

*__Corresponding author:__ aqeelshah@cloud.neduet.edu.pk, wenliu@mail.buct.edu.cn

Original Research

Received:
25 June 2024
Revised:
01 August 2024
Accepted:
23 August 2024
Published online:
08 October 2024

Abstract:

Wastewater containing toxic compounds poses health hazards to living beings. Current research focuses on the degradation of malachite green (MG) as a hazardous pollutant dye by using tire scrap-derived activated carbon (AC) to develop nanocomposites with ZnO by hydrothermal method. The morphology, crystal quality, electrochemical active surface area (ECSA), EIS, antibacterial activity, and optical and photo luminance aspects were studied. The morphology was studied by SEM. The crystalline and elemental composition study was performed using XRD and FTIR, respectively. UV-visible spectroscopy and photoluminescence were employed for optical studies. The ZnO@C nanocomposite exhibited a nanorod-like shape and hexagonal phase. The role of AC in ZnO@C composite was investigated for the removal of MG under UV illumination. Results exhibited that the degradation rate for MG was highly dependent upon dye concentration and pH. Furthermore, an antibacterial study was performed on the nanocomposites. A significant reduction in the band gap (12.6%) was achieved with excellent degradation efficiency of 100%. These results suggest that tire scrap waste could produce a new class of carbon materials for various applications, especially in the energy, environment, and biomedical sectors.

Keywords: Activated carbon (AC); Antibacterial activity; Malachite green; Photodegradation; Tire scrap; ZnO nanocomposite

1. Introduction

Water is essential for preserving life. However, most of the water on earth is too salty to be suitable for most human activities, and pollutants from anthropogenic causes have decreased freshwater quality [1]. Fresh water should be sufficient in quantity and quality [2]. Besides domestic use, industries are prime consumers of fresh water. Industries like textile, paper, tanning, leather, dye, pigment, phar-

maceutical, and food produce vast amounts of wastewater [3, 4]. Surface and groundwater sources include many contaminants, such as coliforms, toxic trace metals, and a wide range of organic and inorganic pollutants [5]. According to the World Bank report, a significant portion of freshwater, i-e 20%, is used in textile processing, significantly contributing to wastewater generation. These effluents contain high concentrations of heavy metals, non-biodegradable organics, phosphates, organic dyes, salts, and suspended particles [6], leading to health hazards. MG is among the widely consumed colorants in various industries like textile, food, and paper [7]. It is a toxin that affects multiple organs, as observed in clinical and experimental studies. Furthermore, it was noted that exposure to MG resulted in an elevation in the count of white blood cells (leukocytosis), a delay in the blood coagulation process, and other issues like increased heart rate, headaches, and eye irritation [8]. As a result, the focus should be given to its effective removal from wastewater.

Numerous techniques have been employed to address wastewater treatment, including coagulation, chemical precipitation, oxidation, absorption, filtration, and ion exchange [9]. However, several issues are associated with them; some are costly, some need larger volumes, others are material dependent, some involve pretreatment, and some are highly complicated and have the capacity to produce reactive oxygen species when exposed to UV light. The photocatalytic degradation technique offers promising results by involving nanomaterials co-catalysts to remove pollutants [10]. Different synthesis methods have been addressed using a variety of approaches to create UV/visible light (VL) driven nanocomposite photocatalysts for environmental applications [11]. Strongly oxidizing, stable, affordable, and non-toxic properties are among these photocatalysts' key advantages, assuming that the processes are run at room temperature and pressure. Due to the way their bands are structured, photocatalysts absorb light at proper wavelengths [12]. As a result, several tactics are needed to effectively use these photocatalysts, including raising the charge carrier transfer rates of photocatalysts and decreasing the electron-hole recombination rate to create extrinsic band gaps with lower energies [13, 14]. The SSA of nanomaterials is a crucial factor that affects photocatalytic activity [15, 16]. Researchers have recently focused on creating a novel photocatalyst that can degrade dyes exposed to visible light in a less hazardous, reusable, and cost-effective manner [17]. In a typical photocatalytic process, the photocatalyst's ability to harvest light, the effective separation of photoinduced electron-hole pairs, and the pollutant adsorption to the active sites on the catalyst's surface are all well-known essential regulating elements. Consequently, the light source and photocatalytic substance are essential variables [18, 19]. Effective use of the light source depends on the nature and structure of the photocatalyst. So, the most essential element in every photocatalytic process is the employed photocatalyst. A semiconductor photocatalyst's photogenerated electron-hole pairs further break down pollutant molecules when exposed to gentle light [20, 21]. Among different photocatalysts, ZnO has been the choice of many researchers due to its low cost, ease of recovery, abundance, and ability to generate reactive oxygen species under UV light [22]. However, there are limitations associated with ZnO, like recombination rate, limited stability, aggregation, and wide band gap, leading to its limited efficiency in the removal of pollutants [23]. Adding elements in ZnO nanoparticles to form composites can enhance their photocatalytic activity by altering their electronic band structure, which increases the separation of the electron-hole pairs and improves the charge transfer efficiency, leading to enhanced photodegradation [17]. Therefore, adding elements is crucial to improve the degradation efficiency of ZnO. The activated carbon exhibits unique and attractive properties like porosity, substantial surface area (SSA), and non-toxic, inexpensive substances with excellent performance [24, 25]. The Hydrothermal technique-assisted synthesis of metal oxide semiconductors has been considered a preferred choice for the photocatalytic degradation of wastewater [26]. It has several advantages compared to the other conventional techniques for material synthesis, like cost-effectiveness, energy saving, simplicity, better nucleation control, increased dispersion, pollution-free, enhanced morphological control, higher rate of reaction, and low operating temperature in the presence of an appropriate solvent. Moreover, it is facile, environmentally friendly to a larger extent, and tunable with growth parameters such as pressure, temperature, pH of the solution, and precursor concentrations; thus, the desired nanostructures are easily achievable [10].

In addition to dye degradation, bacterial infections are now recognized as a worldwide severe hazard to human health because of the emergence and swift dissemination of these microorganisms, especially in pediatric patients. Determining new antibacterial agents to combat strains of bacteria, particularly food pathogens like Salmonella types, *Clostridium perfringens*, *Escherichia coli*, *Campylobacter jejuni*, *Pseudomonas aeruginosa*, *Staphylococcus aureus*, and *Enterococcus faecalis*, has become imperative [27]. The employment of inorganic antimicrobial agents has gained attention in the fight against infections due to their significant benefits over organic antimicrobials, including reduced host toxicity, increased stability over extended periods, decreased microbial resistance, and superior selectivity [28]. Compared to other inorganic antimicrobials, (ZnO) has additional benefits like reduced cytotoxicity, improved selectivity, increased stability, and heat resistance [29]. Various alternate tactics have been employed recently to increase ZnO NP stability and enable its dispersion in aqueous media [30]. The way that nanoparticles (NPs) interact with bacteria cells can be modified by their surface characteristics, which can also impact the antimicrobial activity of ZnO NPs [31, 32]. Cepin et al. [32] reported positive outcomes of the impact of various silane-based surface modifiers on ZnO NP's antibacterial activity against *S. aureus* and *E. coli* bacteria.

The proposed study offers the facile synthesis of AC using tire scrap, which reduces the optical band gap of ZnO using different AC contents. And the role of AC content variation in developing the various nanocomposites for the efficient degradation of dye. The existing literature has not realized such aspects of AC in the design of ZnO@AC nanocompos-

ites. To the best of our knowledge, no research has been conducted on using AC derived from scraped tires as a co-catalyst for the photodegradation of MG dye. In this study, AC was derived from scrap tires using the pyrolysis method. However, there are many ways to recycle waste tires; pyrolysis has drawn lots of attention from industries recently because it converts waste tires into organic compounds that can be used at high temperatures without oxygen. About $30-40\%$ of the weight of pyrolytic char is recovered using this environmentally friendly process [33]. When steam, nitrogen gas, or CO_2 are present, and the pyrolytic char is recovered, AC can be produced at high temperatures and applied as support to deposit ZnO nanostructures, and a nanocomposite was developed during the hydrothermal process. The addition of AC reduced the optical band gap of ZnO, leading to the efficient degradation of MG due to the extensive exploitation of photons under UV illumination. The results obtained from several investigations on the photocatalytic degradation of MG dye are presented in the Table in subsection 3.6. It is evident from these findings that the newly developed ZnO@C nanocomposites are more effective in eliminating MG dye. Furthermore, these nanocomposites display notable antibacterial properties.

2. Materials and methods

2.1 Chemical reagents

The chemicals, such as zinc nitrate hexahydrate ($H_{12}N_2O_{12}Zn$), hexamethylene tetramine ($((CH_2)_6N_4)$), potassium hydroxide (KOH), acetone ($((CH_3)_2CO)$), methanol (CH_3OH), and ethanol (C_2H_5OH), were obtained from Sigma Aldrich, Karachi, Sindh, Pakistan, and utilized in as received condition.

2.2 Synthesis of activated carbon

Scrap tire (Honda Bike Model: CD-70,2016) was collected from a local bike workshop near NED University, Karachi. It was then ground and sieved to sizes of $1-4$ cm; after washing gently, scrap pieces were dried in an oven (DZF-6050-HT, MTI Corporation) for 24 hours at 110 °C temperature before the pyrolysis process. As the raw material, tire char contains 85 percent carbon, sufficient to operate a pyrolysis pilot plant. After re-treating the scrap tires by fixing the average temperature to 450 °C of the pyrolysis reactor, we can produce fuel gas such as hydrocarbon fuel and tire char [33]. To develop the activation process, the nitrogen gas (99.7% pure) was purged into the furnace with a flow rate of 100 mL/30 s to eliminate other gases from the furnace. Before the furnace was allowed to achieve the desired activation temperature from 900 to 975 °C in the presence of nitrogen gas, it was loaded with 30 g tire char. Steam and nitrogen with a ratio of 85:15 was injected into the activation furnace with a 350 mL/30 s flow rate with the help of a peristaltic pump when the required activation temperature was achieved. The activation process can run up to 2 to 6 hours to develop various porous structures [34]. Finally, AC was completed as a black product, as shown in S1.

2.3 Synthesis of pure ZnO nanoparticles and various AC-assisted ZnO@C nanocomposites

Zinc oxide nanostructure synthesis was performed using the hydrothermal method in the following two steps [4].

a. Seed solution: At first, to prepare the pure and AC-assisted ZnO nanostructure, a 200 mL beaker was taken. A 109 mg KOH was taken and dissolved into a 65 mL methanol solution and sonicated for 30 min. The resultant product was labeled as solution B. Next, another solution, labeled as solution-A, was prepared by dissolving 274 mg of zinc acetate into 125 mL of methanol on a heated magnetic stirrer plate at 60 °C for two hours. Simultaneously, after a brief 30-minute interlude, the captivating solution-B was added into solution-A, drop by drop, employing a delicate stirring technique within 20 to 25 min. After completion of two hours, solution-A was ready and termed as seed solution.

b. Growth solution: The growth solution was the next solution prepared and termed solution-C. A 200 mL glass

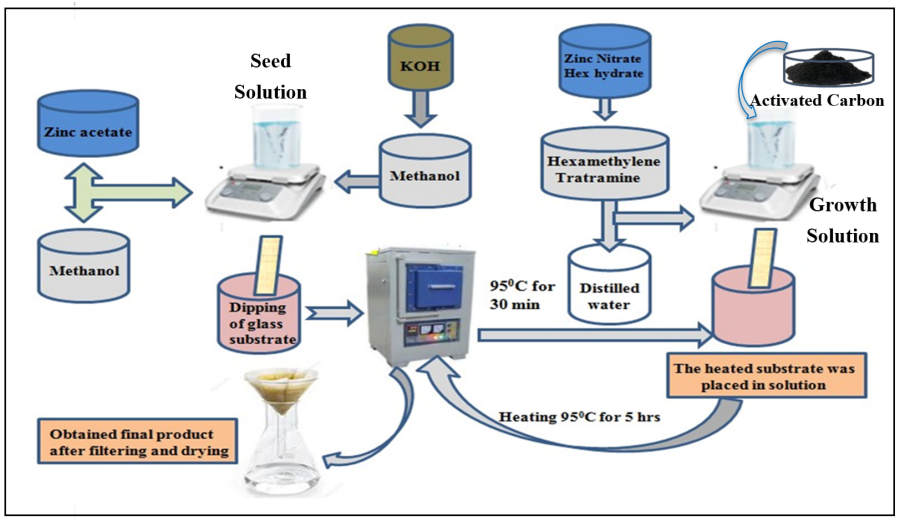

Scheme 1. Detailed schematic diagram for synthesizing pure ZnO nanoparticles and AC-assisted ZnO@C nanocomposites using the hydrothermal method.

beaker was taken and purged using distilled water and acetone; next, 2.22 g of zinc nitrate hexahydrate and 1.05 g of Hexamethylene tetramine were added. Finally, 100 mL of distilled water was added, followed by stirring for 30 minutes at room temperature. Meanwhile, five glass slides were cleaned with acetone, followed by a thorough drying process. Subsequently, each of the five slides was immersed separately into the seed solution $3-4$ times each, followed by annealing at 130 °C for 30 min. The annealing process ensures the proper adhesion of the seed layer. Finally, two solutions, namely the seed solution (solution B) and the growth solution (solution C), were successfully prepared. Five beakers were prepared to serve as growth solutions and were labeled as pure ZnO, 2 mg, 4 mg, 6 mg, and 8 mg, respectively. The AC acquired from the scraped tyre was subsequently introduced into the four labelled beakers, each with AC concentrations of 2 mg, 4 mg, 6 mg, and 8 mg, respectively, into the growth solutions.

Each beaker was covered with aluminum foil to prevent evaporation and was placed inside the oven at 95 °C for 4 hours. Subsequently, the specimens were removed from the oven, and the resulting solution was filtered after room temperature was achieved. A white substance consisting of ZnO nanoparticles was obtained from the beaker labeled as pure, while slightly dark ZnO@C nanocomposites were obtained from the 2 mg, 4 mg, 6 mg, and 8 mg designated beakers. The recipe for synthesizing pure ZnO nanorods and ZnO@C nanocomposites is depicted in Scheme 1. The powder X-ray diffraction (XRD) was applied using Bruker D8-Phaser, CuKα1, (λ = 1.5406 Å). Scanning electron microscopy (SEM) was employed at 10 kV accelerating voltage to study the shape structure of prepared materials. The functional group analysis was done by using Fourier transform infrared spectroscopy (Tensor 27, Bruker Optics FT-IR, Karlsruhe, Germany). The UV-visible for optical band calculations absorbance of the mixture and degradation efficiency was measured using UV-Vis spectroscopy (PE Lamda356).

2.4 Photocatalytic measurements using various ZnO@C nanocomposites

The photocatalysis of newly synthesized samples was performed to degrade MG using UV light (40 W UV lamp, 365 nm). At first, pure ZnO, pure AC, and various ZnO@C nanocomposites prepared with a different mass of AC, such as 2 mg, 4 mg, 6 mg, and 8 mg, were separately added into six beakers, each containing 50 mL distilled water and 10.9×10^{-5} M of MG solution. It was sonicated (10 min) in the dark to obtain a homogenous mixture. Two different MG concentrations were used, 10.9×10^{-5} M and 8.22×10^{-5} M, to study the effect of the initial dye concentration upon the photocatalytic activity of newly prepared materials. Secondly, the solution was irradiated under UV light at various irradiation times from 15 to 210 minutes with an equal interval of 15 min.

2.5 Antibacterial measurement of various ZnO nanocomposites

The antibacterial activity was performed by following the procedure:

At first, eight petri plates, two cotton swabs, and 6 test tubes were autoclaved. Media (Nutrient agar and Nutrient Broth) were prepared and, after autoclaving, poured into the sterile petri plates. Pre-incubation of the plates at 37 °C for 24 hours is followed. *E. coli* and *S. aureus* cultures were inoculated onto nutrient broth and subsequently subjected to a 24-hour incubation period at 37 °C. After 24 hours, *E. coli* and *S. aureus* lawns were prepared on pre-incubated Nutrient agar plates (4 plates for each culture) in a sterile environment [35, 36]. Three wells on each plate were then created using a sterile borer. 1:100 dilution of each sample, i.e., pure ZnO and AC, and various ZnO@C nanocomposites prepared with a different mass of AC, such as 2 mg, 4 mg, 6 mg, and 8 mg, were prepared. These wells were then filled with 0.01 mL of dilutions of given samples on both cultured plates for each sample. A 24-hour incubation period at 37 °C was observed for the plates. Once twenty-four hours had passed, all the plates were ready for observation (see S2).

3. Results and discussion

3.1 Characterization of ZnO@C nanocomposites

The crystalline characteristics of pure ZnO and various ZnO@C nanocomposites were studied using powder XRD. The recorded reflection patterns are depicted in Fig. 1. Typical diffraction patterns of ZnO with hexagonal phase (100), (002), (101), (102), (110), (103), (200), (112), (201), (004), and (202) were observed at two theta angels 32°, 33°, 36.2°, 47.5°, 56.4°, 63°, 66°, 67.8°, 69°, 72.7° and 77° respectively. In each nanocomposite sample, the ZnO crystal arrays were highly intense and prominent, indicating the dominance of ZnO in crystalline properties, whereas the AC material, being amorphous, did not show any obvious reflection. The ZnO nanocomposite was prepared with different masses of AC, like 2, 4, 6, and 8 mg, and their crystalline properties were compared with pure ZnO, as depicted in Fig. 1. Each sample exhibited the hexagonal crystal phase, as confirmed by the diffraction patterns that corresponded precisely to standard JCPDS card no. 01-079-0207 [37].

The average crystallite size of the NPs from the X-ray line broadening of the diffraction peaks and estimation of lattice strain by using Debye Scherrer's formula Eq. (1) and

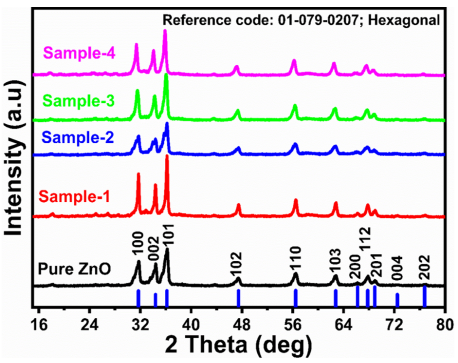

Figure 1. Distinctive powder XRD patterns of various AC-assisted ZnO@C nanocomposites and their comparison with the pure ZnO.

Table 1. Structural parameters of pure ZnO and various AC-assisted ZnO@C nanocomposites.

Sample: ID	hkl	FWHM β (°)	Peak Position 2θ (°)	Height	Av. Crystalline size (nm)	Av. Strain (ε) $\times 10^{-3}$
Pure ZnO	100	0.27263	31.04461	215.64282	28.805	4.17
	101	0.30532	36.26161	948.80022		
Sample-1	100	0.26302	31.71061	1057.20106	29.655	4.02
	101	0.29927	36.18761	1583.9062		
Sample-2	100	0.46635	31.74761	478.57422	19.405	6.22
	101	0.396	36.18761	809.1198		
Sample-3	100	0.39159	31.37761	811.2588	20.5	5.9
	101	0.41888	35.85461	1161.0071		
Sample-4	100	0.52167	31.52561	788.52627	15.93	7.52
	101	0.52051	36.07661	1185.87139		

Williamson-Hall's formula Eq. (2), respectively [38, 39]. The measured structural parameters [40] are given in Table 1.

$$\text{The average crystallite size D} = \frac{0.9\lambda}{\beta \cos\theta} \tag{1}$$

$$\text{Strain } \varepsilon = \frac{\beta}{4\tan\theta} \tag{2}$$

where λ is the wavelength of the X-ray used (1.5406 $\AA$), β is the angular peak width at half maximum, and θ is Bragg's diffraction angle. The calculated average crystallite size of the ZnO NPs is 15.93 nm. The measured cell parameters (a = 2.4736 $\AA$ and c = 6.9508 $\AA$) and volume (V = 47.15 $\AA^3$) of ZnO NPs are smaller than that of bulk ZnO structure (a = 3.2568 $\AA$, c = 5.2125 $\AA$ and V = 47.88 $\AA^3$). The noticed contraction in the lattice parameter is because of the size effect.

FT-IR measurements were conducted on Pure ZnO and AC-assisted ZnO@C nanocomposites (sample-1, 2, 3, and 4), covering the wave number range of $400-4000$ cm^{-1}, as given in Fig. 2. The peaks identified within the $600-400$ cm^{-1} region are attributed to Zn-O vibrations of all pure ZnO and AC-assisted ZnO@C nanocomposites samples [41]. The O-H stretching vibrational mode is characterized by a spectral band between 3090 and 3517 cm^{-1}, arising from water and Zn-OH [42]. Moreover, at 1450 cm^{-1}, the stretching modes corresponding to symmetric and asymmetric C=O bonds are observed. In contrast, the band at 885 cm^{-1} is associated with the C-H out-of-plane bending of pure ZnO and AC-assisted ZnO@C nanocomposites [43]. The peaks observed at $1680-1822$ cm^{-1}, originating from the stretching vibrations of the C=O group and medium bands of -C-C- (aromatics), were detected at 172.33 and 1041.89 cm^{-1} [44]. Consequently, the FT-IR spectra of every sample of pure ZnO and AC-assisted ZnO@C nanocomposites depicted in Fig. 2 exhibit minimal discrepancies among all spectra (which resembles XRD data), indicating that no chemical interaction occurs between ZnO and AC. The structure and shape of different ZnO@C nanocomposites prepared with AC were studied through low-resolution SEM, and their shape orientation was compared with the pure ZnO, as given in Fig. 3. The morphology of as-prepared ZnO nanocomposites is oriented randomly with nanorod-like morphology. The diameter of the nanorod was observed to be from $200-300$ nm, as given in Fig. 3 a-d. The pristine ZnO exhibited a similar shape orientation to the nanorod, suggesting that using AC could not change the morphology of ZnO in each nanocomposite system, as shown in Fig. 3 e. AC morphology was also studied, and

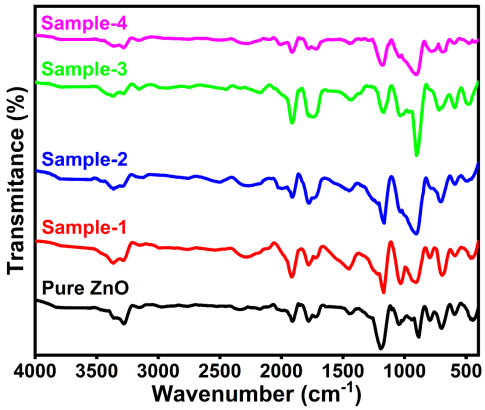

Figure 2. Distinctive FTIR spectra of pure ZnO and various AC-assisted ZnO@C nanocomposites.

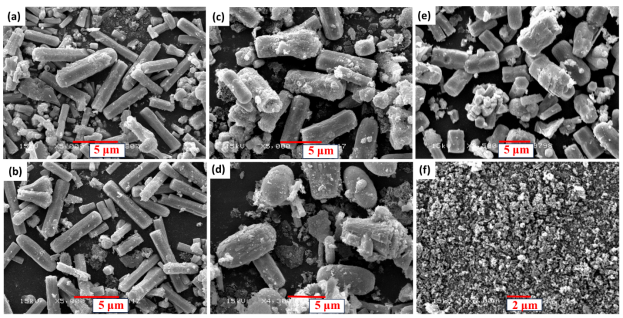

Figure 3. SEM images for different AC-assisted ZnO@C nanocomposites using different mass concentrations of AC (a) 2 mg, (b) 4 mg, (c) 6 mg, (d) 8 mg, (e) pure ZnO, and (f) pure AC.

fine particles with high porosity were observed, as shown in Fig. 3 f. It is evident from the SEM analysis that the AC had exhibited a negligible effect on the alteration of ZnO morphology. Its presence in the nanocomposites could enable favorable dye degradation. The EDS was carried out for the identification of elements present in the pure AC, pure ZnO, and ZnO@AC composites with 2 mg, 4 mg, 6 mg, and 8 mg concentrations, as shown in Fig. 4 a-f. The EDS spectra revealed the elements as given: C in pure AC, Zn, and O in pure ZnO, and C, O, and Zn in AC-assisted ZnO@C nanocomposites in varying mass percentages, as shown in Fig. 4 a-f. The presence of C in AC-assisted ZnO@C nanocomposites reveals a successful incorporation of AC in AC-assisted ZnO@C nanocomposites. It was further observed that there was an increase in the mass percentage of carbon with the increase in the concentration of AC from $2-8$ mg.

TEM analysis was also performed, and the corresponding TEM images of pure ZnO and its composites with different AC contents are shown in S3 a-e. This analysis suggests that the surface morphology of ZnO was almost the same as that of SEM results. However, using AC brought some carbon content texture on the surface of ZnO, as shown in S3 a-e.

The optical band gap analysis was done to understand the role of AC in the alteration of the band gap value of various mass concentrations of AC in ZnO@C nanocomposite. The results obtained were compared with the energy gap value of pure ZnO, as shown in Fig. 5. For this purpose, we used the UV-visible absorbance spectra of nanocomposites and pure ZnO, as given in Fig. 5 a. The bandgap value of semiconducting material is critical when studied for photocatalytic applications. The corresponding Tauc. Plots of various ZnO@C nanocomposites and pure ZnO were estimated using absorbance spectra in the UV-visible range, as given in Fig. 5 b-f [45].

The pure ZnO experienced a typical bandgap value of 3.15 eV. In contrast, as the concentration of AC increased, a persistent decline in the optical band gap was noted. For various mass concentrations of AC in ZnO nanocomposites, namely, 2, 4, 6, and 8 mg possessed the energy gap value of 2.96 eV, 2.90 eV, 2.82 eV, and 2.73 eV, respectively, as shown in Fig. 5 c-f. An appreciable decrease in the energy gap of about 12.6% was achieved for maximum AC content (8 mg). The reduction in band gap has offered the rapid charge transfer with a minimum recombination rate. Hence, the degradation significantly increased. Here, the energy gap would provide the opportunity for extensive exploitation of photons, which can further enhance the photocatalytic efficiency.

An investigation of the impact of AC on the luminescence characteristics of ZnO was additionally conducted using PL. The excitation wavelength of 320 nm of photons was used during the operation of the photoluminescence, and the corresponding PL spectra of different AC-assisted ZnO@C nanocomposites and pure ZnO were recorded as shown in S4. Each sample showed several emission peaks in the visible part, and they could be connected to several defects, such as oxygen defect levels. The strong and weak emission bands located at $400-500$ nm are linked to the deep-level emissions [46]. The nature of defects could be either oxygen or zinc vacancies. The relatively strong emissions were observed for the ZnO@C nanocomposites compared to the pure ZnO, as given in S4. The use of AC in ZnO has shown more substantial emissions at 521 and 543 nm. The green emission band was indexed to zinc vacancies. Moreover, the green/yellow emission bands were found at 570 nm and 596 nm due to the intrinsic defects of ZnO, as given in S4. The green emission band was indexed to zinc vacancies [47]. Moreover, the green/yellow emission bands were found at 570 nm and 596 nm due to the intrinsic defects of ZnO, as shown in S4.

3.2 Photocatalytic applications of ZnO@C nanocomposites

As depicted in Fig. 6, the initial investigation involved observing the photodegradation of MG under UV light irradiation for 210 minutes without employing any catalyst. It

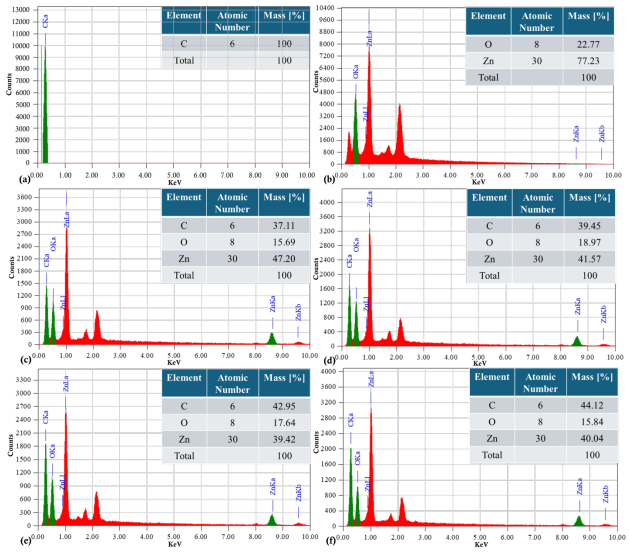

Figure 4. EDS spectra and mapping (a) pure AC, (b) pure ZnO, (c) 2 mg of AC-assisted ZnO@C, (d) 4 mg of AC-assisted ZnO@C, (e) 6 mg of AC-assisted ZnO@C, and (f) 8 mg of AC-assisted ZnO@C.

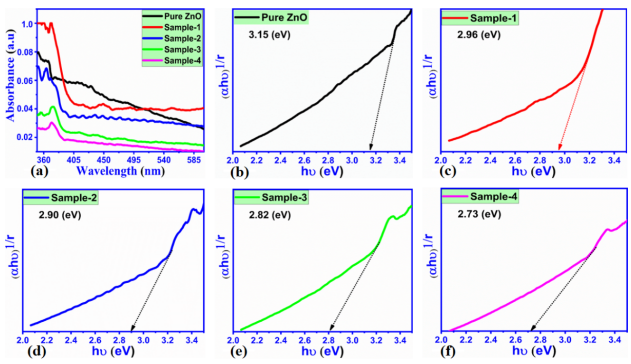

Figure 5. UV-visible absorbance spectra for (a) pure ZnO and different AC-assisted ZnO@C nanocomposites prepared with mass concentrations 2,4,6 and 8 mg of AC, (b-f) their corresponding Tau plots.

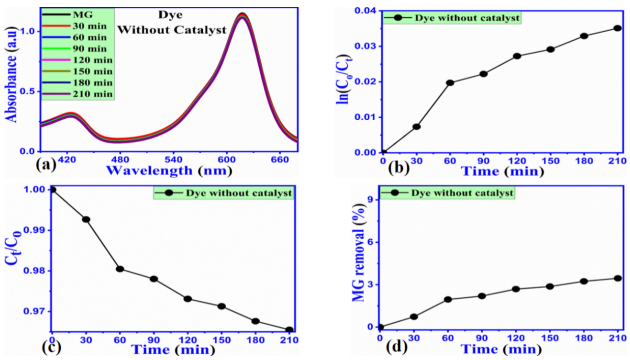

Figure 6. (a) UV-visible absorbance spectra of MG elimination with the illumination of UV light, (b, c) degradation kinetics of MG without the catalyst, and (d) degradation efficiency of MG under UV irradiation.

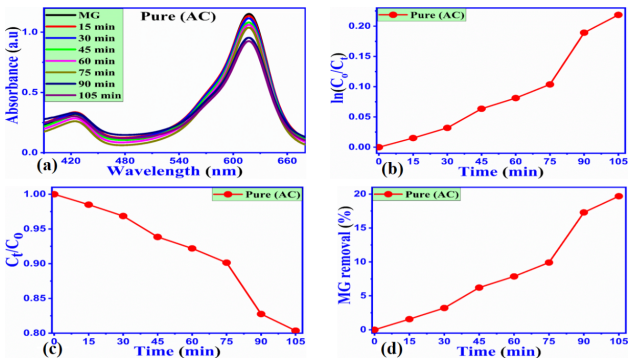

Figure 7. (a) UV-visible absorbance spectra for pure AC, (b, c) degradation kinetics of MG, (d) degradation efficiency of MG.

is evident from the spectra examined at different intervals that the reduction in the absorbance spectra was negligible, proposing that UV light could not effectively degrade the malachite green as depicted in Fig. 6 a. Hence, an efficient and stable photocatalyst is highly beneficial for properly treating wastewater pollutants. The photodegradation kinetics of the MG were also studied without using a catalyst, and it is obvious that observed rate constant values were minimal, indicating the slow degradation rate followed by first-order kinetics [48]. The elimination rate was mainly dependent on the MG concentration and independent of water; hence, in the rate-determining step, only malachite was going under the chemical change, as given in Fig. 6 b-c. The elimination efficacy of MG without photocatalytic dose was estimated, and the obtained value was about 3%, which is negligible, as shown in Fig. 6 d. Therefore, the researchers are concentrating on fabricating a new generation of light-activated catalysts to meet the water pollution challenges caused by synthetic dyes.

According to Grotthus-Draper's law, the rate of a normal photodegradation process is determined by the quantity of absorbed photons. At time "t," the rate is under constant illumination. The number of photons absorbed by the reactants decreases as the photodegradation process proceeds because fewer photons are absorbed by the degradation products when they can absorb them. Under these circumstances, the amount of light that has been absorbed by the solution is often more substantial compared to that of the reactants. The Langmuir–Hinshelwood model could be used to infer the reaction parameters of the photodegradation process [48, 49].

$$\frac{dC}{dt} = kC_t \tag{3}$$

After solving simple mathematics steps according to photodegradation processes, we have:

$$\ln\left(\frac{C_t}{C_o}\right) = k_{app} \times t \tag{4}$$

While C_o signifies the initial concentration of the dye in milligrams per liter at time zero, C_t denotes the concentration of the dye in milligrams per liter at a particular reaction time, t. k_{app} signifies the constant that represents the rate of the reaction.

Also, we have used Eq. (5) to obtain photodegradation efficiency.

$$\text{PDE\%} = \frac{I_o - I_t}{I_o} \times 100 \tag{5}$$

where I_o represents the starting dye absorbance (a.u), I_t exhibits the dye absorbance (a.u), when exposed to ultraviolet light at various intervals.

Pure scrap tire-derived AC was employed in the MG solution to observe its photocatalytic activity under UV illumination, as given in Fig. 7. Without a catalyst, the decline in absorbance spectra was comparatively more significant than the dye removal, as depicted in Fig. 7 a. This indicated that the AC offers its role in removing pollutants due to its porous and fine particle size; hence, dye removal is relatively better due to the combined effects of adsorption and catalytic oxidation. The rate constant values and first-order degradation kinetics were marginally higher than the dye degradation in the absence of the catalyst, confirming the increase in the removal rate in the existence of AC catalyst dose 5 mg/50 mL, as given in Fig. 7 b-c. The dye removal was also calculated, and the obtained value of 19% was noticed, as shown in Fig. 7 d. The removal of MG using pure scrap tire-derived AC is still insufficient; hence, a new generation of catalysts is needed to work efficiently for wastewater treatment. Besides the bare active carbon obtained from the tire scrap, we have also studied the photodegradation of MG using pure ZnO (5 mg/50 mL). The corresponding absorbance spectra of MG removal were measured for the 15-minute time interval up to 105 min, as given in Fig. 8 a. The absorbance decrease was 40% efficient, much higher than bare AC and dye degradation without the catalyst. Hence, it is believed that ZnO has a high potential for use in photocatalytic applications. However, the efficiency of pure ZnO was still insufficient, corresponding to the fast neutralization of ions (electron and hole pairs) and having a wide optical band gap. The degradation kinetics of MG was also studied, and the degradation rate was expressed in Fig. 8 b, c. Its degradation efficiency is given in Fig. 8d.

Therefore, we have designed and applied a new class of photocatalysts, i.e., ZnO@C nanocomposites based on scrap tire-derived AC, to remove MG under UV illumination.

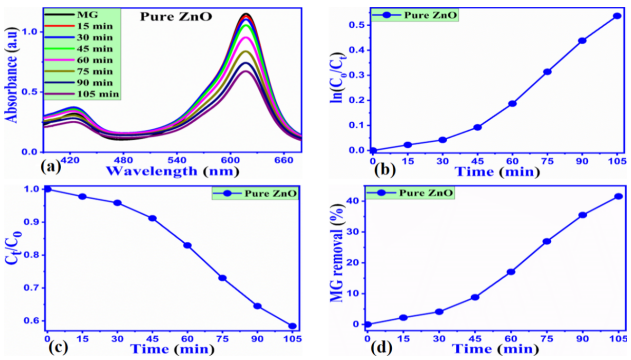

Figure 8. (a) UV-visible absorption spectra for pure ZnO, (b, c) degradation kinetics of MG, (d) degradation efficiency of MG.

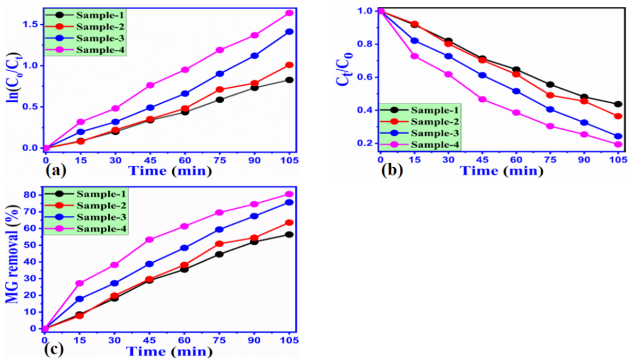

Figure 10. (a, b) degradation kinetics of all AC-assisted ZnO@C nanocomposites in 10.9×10^{-5} M MG aqueous solution, (c) Degradation efficiency of all AC-assisted ZnO@C nanocomposites.

Four composite samples were formed with different concentrations of AC in ZnO and were named sample 1 (2 mg), samples 2 (4 mg), samples 3 (6 mg), and sample 4 (8 mg), respectively, and were applied (with fix catalytic dose 5 mg/50 mL) separately for the removal of 10.9×10^{-5} M MG under UV light illumination. An analysis was conducted on the UV-visible absorbance spectra specific to each sample, as given in Fig. 9 a-d. It was noticed that an enhancement in degradation efficiency of about 52% for sample 1, 55% for sample 2, 72% for sample 3, and 81% for sample 4 was achieved, as shown in Fig. 10 c. These results verified that the increasing content of AC in the ZnO nanocomposite exhibited significant photocatalytic activity; hence, endorsing the role of AC in the development of ZnO@C nanocomposite is vital. This is because, with increasing AC content in the composite system, the absorbance successfully decreased, which could be assigned to an excellent photodegradation rate.

The contribution of AC in the performance of nanocomposite systems could be ascribed to the large surface area of AC that synergistically enhanced the photocatalytic performance of ZnO. Using waste tire carbon in producing carbon-based materials presents a promising strategy for advancing photocatalysts of subsequent generations, which could be implemented in practical applications such as hydrogen generation and wastewater treatment. The kinetics of degradation for the ZnO@C nanocomposites were also examined, as depicted in Fig. 10 a, b. The findings revealed that the degradation rate became faster with increasing mass concentration of AC in the nanocomposite. At the same time, the rate constant value for the sample 4 was the highest. The kinetics of degradation followed first-order kinetics.

Furthermore, the initial dye concentration was changed from 10.9×10^{-5} M to 8.22×10^{-5} M MG to understand the performance of the ZnO@C nanocomposites was determined to be concentration-dependent, using the same catalytic dose of 5 mg/50 mL as depicted in Fig. 11. It is evident that the absorbance was successively decreasing with increasing the amount of AC in the ZnO@C nanocomposites. Sample 4, with the highest amount of 8 mg of AC, has shown a substantial decrease in the absorbance value, indicating a significant degradation rate. The measurement of UV-visible absorbance spectra in 10.9×10^{-5} M (high concentration) MG has a smaller decrease in the absorbance value compared to in low concentration (8.22×10^{-5} M of MG), as shown in Fig. 11. This comparative results analysis suggests that the photocatalytic performance of AC-assisted the value of initial dye concentration governs ZnO@C nanocomposites. Hence, the present composite sys-

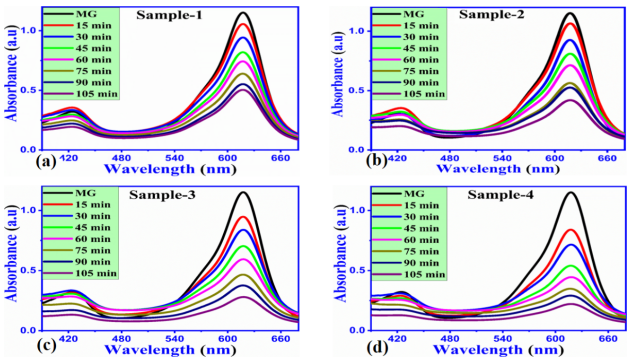

Figure 9. UV-visible absorbance spectra of various AC-assisted ZnO@C nanocomposites in 10.9×10^{-5} M MG aqueous solution (a) sample-1, (b) sample-2, (c) sample-3 and (d) sample-4.

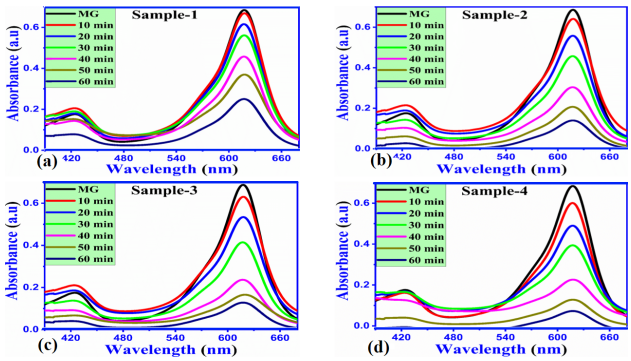

Figure 11. UV-visible absorbance spectra of various AC-assisted ZnO@C nanocomposites in 8.22×10^{-5} M MG under the irradiation of UV light (a) sample-1, (b) sample-2, (c) sample-3, and (d) sample-4.

Table 2. Summarized photocatalytic activities for newly synthesized pure AC, pristine ZnO, and AC-assisted ZnO@C nanocomposites.

Catalyst and its dose	Degradation at high dye Conc. 10.9×10^{-5} M		Degradation at low dye Conc. 8.22×10^{-5} M		Optical band gap (eV)
5 mg/50 mL	Efficiency (%)	Degradation time (min)	Efficiency (%)	Degradation time (min)	
Without catalyst	03	210	–	–	–
Pure AC	19	105	–	–	–
Pure ZnO	40	105	–	–	3.15
Sample-1	52	105	64	60	2.96
Sample-2	55	105	79	60	2.90
Sample-3	72	105	82	60	2.82
Sample-4	81	105	93.78	60	2.73
Sample-4 at pH 3	–	–	85	60	–
Sample-4 at pH 9	–	–	97	30	–
Sample-4 at pH 12	–	–	100	18	–

tems worked very well in the low concentration of MG. The investigation of degradation kinetics was also conducted for all AC-assisted ZnO@C nanocomposites, and a degradation efficiency of up to 93.78% was obtained, as depicted in S5 and Table 2. The kinetics study has demonstrated that the degradation rate is enhanced as the amount of AC in the nanocomposite increases. Simultaneously, the highest rate constant value was observed for sample 4. The degradation kinetics adhered to the principles of first-order kinetics.

3.3 Effect of pH of dye solution on the photocatalytic performance of ZnO@C nanocomposites

The effect of pH on MG dye solution was studied with sample 4 (8 mg) nanocomposite. The pH of the dye concentration was 8.22×10^{-5} M, and the solution was set using concentrated 0.2 M HCl and NaOH aqueous solutions. Three pH adjustments were made in 8.22×10^{-5} M dye solution ranging from 3, 9, and 12, as shown in Fig. 12. The efficacy of a prepared photocatalyst degradation performance is significantly influenced by the pH of the dye solution [50]. Absorbance spectra in the UV-visible range were recorded for pH 3, 9, and 12. as depicted in Fig. 12 a-c.

The MG dye, being cationic, has shown a favorable degradation rate in a high alkaline pH of 12 compared to the low pH of 3 because, in the low pH, there is a significant possibility of repulsion among the cationic and the hydronium ions; hence, the limited degradation rate was noticed in pH-3 as illustrated in Fig. 13. The decrease in the absorbance rate is high at pH-12 compared to pH-9 and pH-3, indicating the degradation kinetics is highly efficient at pH-12, corresponding to the high density of hydroxyl radicals, as shown in Fig. 13 c. The dye degradation rate could be seen with the pH-3, 9, and 12 in terms of time intervals of 60, 30, and 18 min, respectively, indicating the pH-dependent MG degradation rate as given in Fig. 13 a-c and Table 2.

The kinetics of MG degradation were studied with adjusted pH of 3, 9, and 12 in 8.22×10^{-5} M MG solutions, and the obtained results are depicted in Fig. 13 a-b. The data indicates a strong correlation between the rate constant values and the pH of the dye solution, with an estimated high-rate constant occurring at pH 12. The degradation kinetics under different pH environments of dye solution followed the pseudo-first-order kinetics. The degradation rate increased with increasing pH values from 3, 9, and 12, verifying that the highly alkaline pH of MG solution has favored the degradation trend for MG, as shown in Fig. 13 a-b. We have also evaluated the degradation efficiency of sample 4 under the pH environment of 3, 9, and 12 of MG.

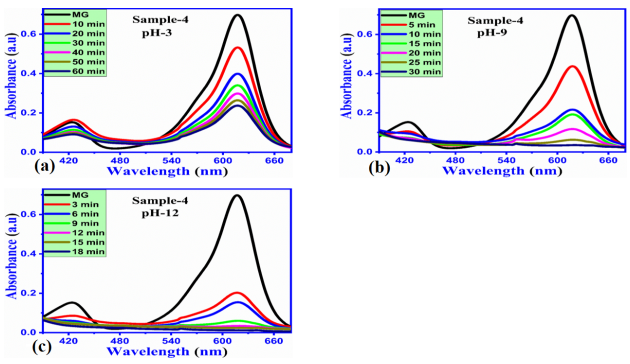

Figure 12. UV-visible absorbance results for 8.22×10^{-5} M MG solution adjusted with (a) pH 3, (b) pH 9, and (c) pH 12 with the use of 10 mg/100 mL catalyst of sample 4 under UV irradiation.

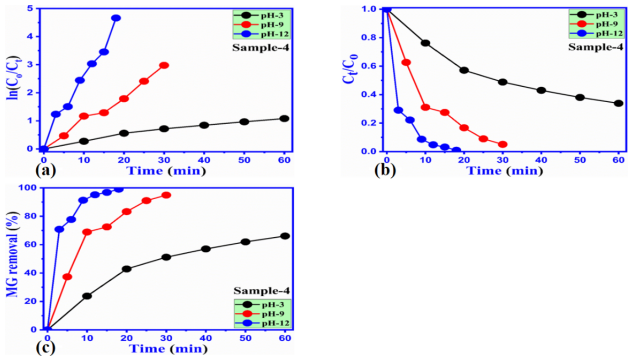

Figure 13. (a) Degradation kinetics at pH 3, 9, and 12 using sample 4 in 8.22×10^{-5} M MG solution (b) C_t/C_o w.r.t time curve for photodegradation (c) Degradation efficiency of MG degradation using sample 4 in different pH values of 3, 9, and 12.

Excellent degradation efficiency of up to 100% for pH 12, 97% for pH 9, and 58% for pH 3 was found, as depicted in Fig. 13 c. The outstanding efficiency of degradation for AC-assisted ZnO@C nanocomposite is shown in Table 2, could be attributed to the synergetic effect between AC and ZnO nanostructures, where AC offered the high possibility of enhanced surface area for the deposition of ZnO nanostructures with maximum exposure of active sites. Significantly, AC decreased the band gap of ZnO, allowing the high exploitation of photons during UV light irradiation. Hence, the outcomes compiled in Table 2 show that the AC-assisted ZnO@C photocatalysts formulated in this analysis showcase extraordinary catalytic performance in eliminating MG from industrial polluted water.

3.4 Reusability and charge transfer of ZnO@C nanocomposite

The stability of the ZnO@C nanocomposite (sample 4) was studied using three repeatable cycle measurements of MG degradation using 8.22×10^{-5} M MG, as shown in Fig. 14. The control measurement was labeled as 0 cycles, and the other three cycles were cyclic stability tests. The reusability test revealed that the ZnO@C nanocomposites revealed significant stability without any appreciable loss of degradation efficiency. Hence, the proposed composite system could effectively degrade MG pollutants.

In addition, the rationale for the extraordinary achievement of the recently produced ZnO@C nanocomposite material in counteracting the deterioration of MG in a water solution was further grasped through the transmission of charge and the ECSA and EIS, as shown in Fig. 15 a–f and Fig. 16. ECSA and EIS were evaluated using the preceding literature [51]. At first, we investigated the magnitude of ECSA from the non-Faradic sector of the cyclic voltammetry (CV) curves that were perceived at various scan rates, as depicted in Fig. 15 a-e. By utilizing the technique of linear fitting to analyze the variation in electrical current densities between the cathode and anode sides of the CV curves, we acquired fitted data that unveiled intriguing slopes, representing the coveted ECSA values mesmerized in Fig. 15 f. The ECSA values were 4.013, 4.210, 5.879, 7.703, and 7.822 μFcm^{-2} for the pure ZnO, samples 1, 2, 3, and 4, respectively.

The significant ECSA value and the reduced charge transfer resistance of the ZnO@C nanocomposites provide robust evidence for their exceptional efficacy in degrading MG dye under UV irradiation.

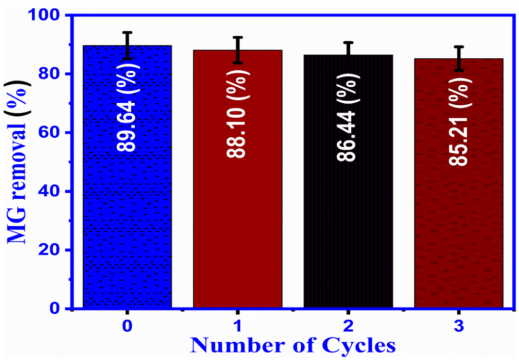

Figure 14. Reusability results of AC-assisted ZnO@C nanocomposites in 8.22×10^{-5} M MG solution under UV illumination.

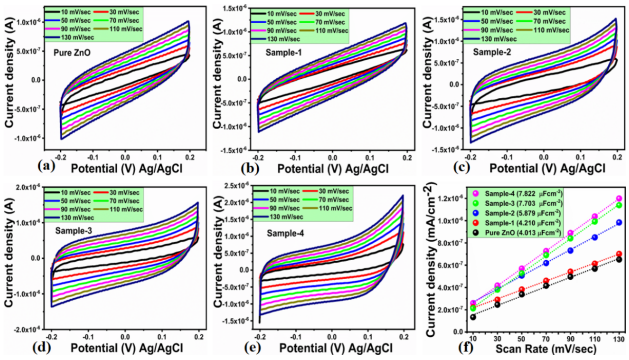

Figure 15. (a-e) Cyclic voltammetry measured in 8.22×10^{-5} M MG solution at different scan rates for all pure ZnO and AC-assisted ZnO@AC nanocomposites, and (f) linear fitting of difference anodic and cathodic current density for measuring (ECSA).

Furthermore, the EIS was performed to analyze the charge transfer, thereby confirming the remarkable deterioration capabilities of the ZnO@C nanocomposite. EIS results provided the quantified measurement of resistance to charge transfer; the corresponding Nyquist plots are depicted in Fig. 16. The construction of the corresponding circuit was accomplished by utilizing components such as the resistance of the solution (R1), the resistance of the ZnO@C nanocomposite material (R2), and the elements with constant phase (CPE1) as shown in Fig. 16. As shown by the Nyquist plots, the modified CPE1 with 8 mg AC has an arc with smaller radius, confirming higher charge transfer for this electrode [24].

The determined resistances for charge transfer of the ZnO@C nanocomposite materials in the MG solution were obtained to be 8.818 Ω, 7.714 Ω, 7.538 Ω, 3.676 Ω, and 2.875 Ω for the pure ZnO, sample 1, 2, 3, and 4, respectively, in the 8.22×10^{-5} M dye solution. These results validate the advantageous charge transfer under UV light during dye

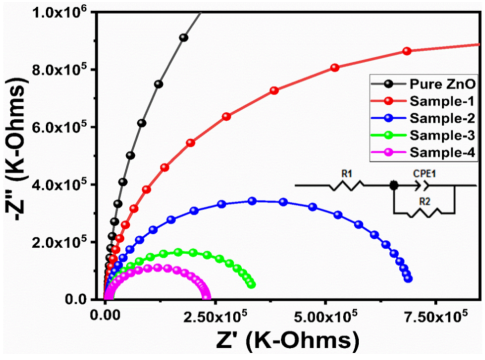

Figure 16. EIS measurement in 8.22×10^{-5} M MG solution and bare water under UV light irradiation at a sweeping frequency rate of 100 kHz to 0.1 Hz, an amplitude of 10 mV, and zero bias potential in open circuit for all pure ZnO and AC-assisted ZnO@AC nanocomposites.

degradation [13]. The ZnO@C nanocomposites propose a decline in the resistance values of 7.714 Ω, 7.538 Ω, 3.676 Ω, and 2.875 Ω for samples 1, 2, 3, and 4, respectively, in comparison to the 8.818 Ω of pure ZnO, as the amount of AC increases. This decrease in resistance value attributable to AC confirms that photogenerated carriers are amplified and interfacial charge transfer is accelerated [52].

3.5 Scavenger study about the verification nature of radicals involved in the degradation of MG

MG's inhibition degradation rate was investigated with a concentration of 10 mM scavengers and 8.22×10^{-5} M MG. Current research delineates the characteristics of the radicals that contribute to the degradation of MG. For this purpose, we studied the role of various scavengers like silver nitrate ($AgNO_3$), ascorbic acid ($C_6H_6O_8$), and ethylenediamine tetraacetate (EDTA) in the vicinity of MG, as depicted in Fig. 17. In the removal of dyes, various radicals have been identified as playing a role in the degradation process of dyes like (O^{2-}) and hydroxyl radicals (OH) [31]. These radicals show the oxidizing properties that oxidize the organic dyes [53]. These chosen scavengers, such as ($C_6H_6O_8$), ($AgNO_3$), and (EDTA), are highly vital to generate the oxidizing radicals and could degrade dye effectively [54]. The scavenger study shows that the silver nitrate has limited the degradation rate of MG; hence, the hydroxyl radicals possibly participated in MG degradation. The advantageous features of the prepared composite system could be briefly described as low cost, facile, high performance, eco-friendly, and environment-friendly. Therefore, when exposed to UV light, it can be a substitute photocatalyst for the MG degradation process.

3.6 Photocatalytic degradation mechanism of MG

On the other hand, the photocatalytic mechanism facilitates the process by which the pores of AC rapidly absorb the dye molecule without light. When exposed to light, the adsorbed solution undergoes decomposition, facilitated by the interaction between water and reactive radicals produced by ZnO under UV light irradiation. In particular, the exposure of the dye solution to UV light radiation, electrons (e^-) situated within the ZnO@C nanocomposites undergo excitation from the valence band (VB) towards the conduction band (CB). This excitation creates holes (h^+) in the valence band [55]. The formation of agglomerations and clusters of ZnO nanoparticles is impeded in this investigation by the existence of an AC matrix. The photocatalytic process is accelerated by the porous characteristics of AC, which increase its surface area and facilitate the infiltration of dye molecules onto the photocatalyst's surface. As a result of the increased surface area caused by the incorporation of AC into the ZnO nanoparticles, a greater quantity of dye molecules is attracted to the photocatalyst. This may result in an increased degradation rate of MG when exposed to UV light. Photocatalytic degradation of dyes according to the proposed mechanism involving AC-assisted ZnO@C nanocomposites is illustrated in Scheme 2. Furthermore, it decreases the distance along which photo-induced charge carriers diffuse, which is a pivotal factor in the photocatalytic mechanism [56]. The electrons captured by AC (possessing a vast surface area and functioning as an effective adsorbent) interact with oxygen (O_2) from the surroundings and water (H_2O) from the solution to generate active radicals such as h^+, O_{2-}^*, and OH^* [26, 57]. The reaction between these superoxide radical anions and the moisture adsorbed on the surface of the photocatalyst yields H_2O_2, which generates additional hydroxyl radicals (OH^*). The complete degradation of MG dye into CO_2, H_2O, and its simpler compounds is attributed to the entities (h^+, O_{2-}^*, and OH^*) produced during the photocatalysis process [58, 59]. The subsequent equations illustrate the progression of MG dye degradation utilizing the prepared photocatalyst [73].

$$\mathrm{ZnO/ZnO@C(Photocatalyst)} + h\nu \rightarrow \mathrm{e^-(electrons)} + \mathrm{h^+(holes)} \quad (6)$$

$$\mathrm{O_2 + e^- \rightarrow O_{2-}^*} \quad (7)$$

$$\mathrm{O_{2-}^* + 2H^+ \rightarrow H_2O_2} \quad (8)$$

$$\mathrm{e^- + H_2O_2 \rightarrow OH^* + OH^-} \quad (9)$$

$$\mathrm{h^+ + H_2O_2 \rightarrow H^+ + OH^*} \quad (10)$$

$$\mathrm{h^+ + OH^- \rightarrow OH^*} \quad (11)$$

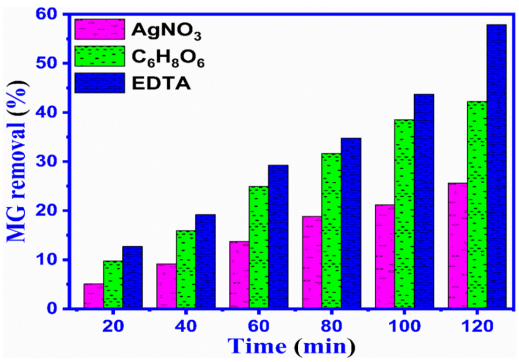

Figure 17. Identifying possible radicals involved in the degradation process of MG using various 10 mM scavengers in the presence of 8.22×10^{-5} M MG solution.

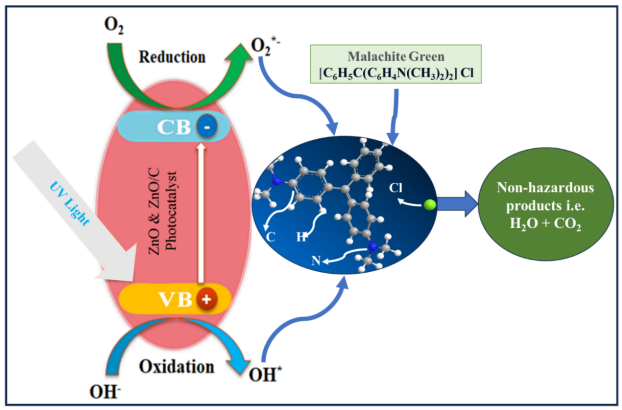

Scheme 2. Schematic illustration for photocatalytic degradation mechanism for pure ZnO and AC-assisted ZnO@C nanocomposites.

Table 3. Comparative analysis of MG photocatalytic degradation by different synthesized photocatalysts.

Photocatalyst	Catalyst Dosage (mg/L)	Dye /Dye concentration	Synthesis Method	Photocat. efficiency (%)	Time of degradation (min)	Source of light	References
MAl_2O_4@AC nanocomposites	50	MG/ 10×10^{-5} M	In situ co-precipitation method	100	90	Visible light	[60]
Ir/ZnO with $K_2S_2O_8$	200	Brilliant Green /0.1 ppm	Chemical method	90	120	Sunlight	[61]
ZnO disc-like spherical NP	150	MG/21.9 mg/L	Precipitation method	92	120	UV light	[62]
Chitosan/Ce-ZnO	50	MG/5 mg/L	Microwave irradiation method	87	90	Visible light	[63]
GO-ZnO/Mn_2O_3	200	MG/50 mg/L	Facile calcination method	98.75	30	Sunlight	[64]
ZnO-β-CD	200	MG/35.5 mg/L	Sol-gel	84	210	Incandescent lamp	[65]
Fe-TiO_2/AC	1000	MG/100 mg/L	Sol-gel	97	45	UV light	[66]
ZnO-NPs	200	MG/10 mg/L	Biosynthesis via Sol-gel & combustion method	99	40	UV light	[67]
BC-TiO_2-ZnO	50	MG/100 mg/L	Sol-gel	98	30	UV light	[68]
TiO_2/$YMnO_3$	150	MG/6.0×10^{-6} M	High-speed stirring technique	95.34	120	Visible light	[69]
SnO_2/ZnO	1000	MG/10 mg/L	Green synthesis	98	150	Xenon lamp	[70]
MoS_2/g-C_3N_4/ZnO	100	MG/10 ppm	Simple exfoliation method	97	60	Visible light	[71]
ZnO/SiO_2	500	MG/10 ppm	Sol-gel	98.17	40	Sunlight	[72]
ZnO@C nanocomposite	100	MG/ 10.9×10^{-5} M	Simple Hydrothermal	81	105	UV Light	Present work
ZnO@C nanocomposite	100	MG/ 8.22×10^{-5} M	Simple Hydrothermal	93.78	60	UV Light	Present work
ZnO@C nanocomposite (pH 12)	100	MG/ 8.22×10^{-5} M	Simple Hydrothermal	100	18	UV Light	Present work

$$\mathrm{MGdye}([C_6H_5C(C_6H_4N(CH_3)_2)_2]Cl) + OH^* + O_{2-}^* + \rightarrow CO_2 + H_2O \quad (12)$$

This process, which generates harmless byproducts, including CO_2 and H_2O [74], involves the reaction of the dyes and organic contaminants and is referred to as photosensitization or photocatalysis. A significant proportion of electrons recombine rapidly with their corresponding holes. However, metal doping has the potential to hinder this process of recombination. In ZnO@C nanocomposites, AC functions as an electron reservoir and engages in charge transfer with the ZnO NPs. This process enhances the photocatalytic activity of ZnO NPs by inhibiting the recombination of electron-hole pairs [80]. Moreover, the outcomes of the photo-catalytic experiments employing various catalysts reported in the literature are compared. These experiments concentrate on removing MG dye, as illustrated in Table 3. The findings obtained in this investigation are also incorporated for comparison.

The results show that this study exhibits tremendous potential in terms of efficacy compared to other studies, particularly regarding UV light irradiation. Moreover, the simple synthesis process and the enhancement of the photocatalytic process suggest that the nanocomposites generated possess prospective applications in domains such as dye-sensitized solar cells, adsorption, and gas sensors.

3.7 Antibacterial activity of as-prepared materials

The antibacterial activity of various samples of AC-assisted ZnO@C nanocomposite and pure ZnO is studied using

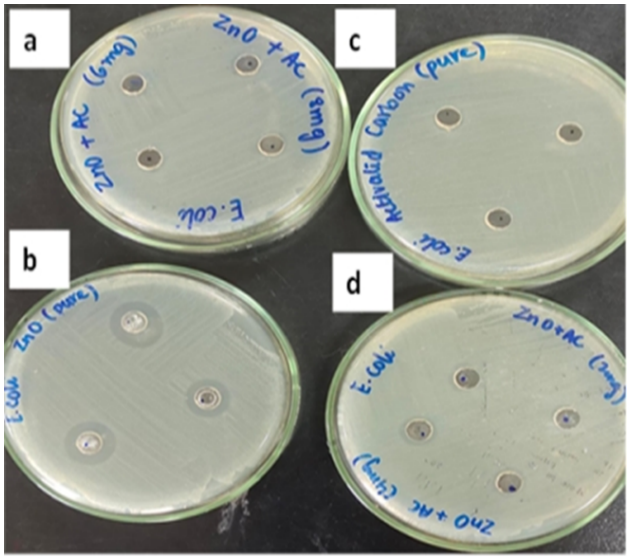

Figure 18. Zone of inhibition of pure ZnO and four AC-assisted ZnO@C nanocomposites (samples 1, 2, 3, and 4) against *E. coli* bacteria.

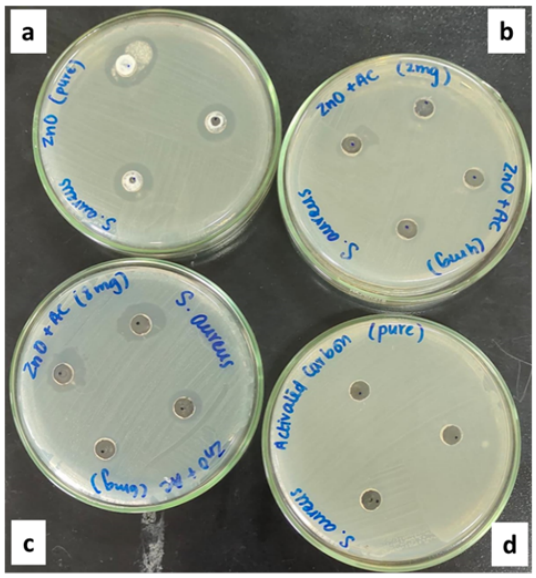

Figure 19. Zone of inhibition of pure ZnO and four AC-assisted ZnO@C nanocomposites (samples 1, 2, 3, and 4) against *S. aureus* bacteria.

Table 4. Comparative analysis of antibacterial activity by different synthesized photocatalysts.

Bacteria	Catalyst and its concentration	Method	Activity or killing rate (%)/ Inhibition Zone (mm)	Ref.
Staphylococcus aureus	ZnO (5 mg/mL)	Agar Method	53%	[75]
Escherichia coli			33.5%	
Staphylococcus aureus	TiO_2 doped ZnO (5 mg/mL)		76.5%	[75]
Escherichia coli			45%	
Staphylococcus aureus	$ZnCl_2/TiO_2$	Inhibition Method	91%	[76]
	$Zn(AC)_2/TiO_2$		82%	
	$Zn(NO_3)_2/TiO_2$		96%	
	$ZnSO_4/TiO_2$		100%	
	($10^4 - 10^5$ CFU/ mL of each)			
Escherichia coli	$ZnCl_2/TiO_2$		93.5%	[76]
	$Zn(AC)_2/TiO_2$		78.5%	
	$Zn(NO_3)_2/TiO_2$		90%	
	$ZnSO_4/TiO_2$		100%	
	(10^4-10^5 CFU/ mL of each)			
Escherichia coli	ZnO/ TiO_2 (25 mg/mL)	Agar Method	18 mm	[77]
Escherichia coli	TiO_2 NPs (200 mg/mL)		16 mm	[78]
Staphylococcus aureus			14 mm	
Escherichia coli	Ag-loaded TiO_2 NPs		08 mm	[79]
Staphylococcus aureus	(40 mg/mL)		04 mm	
Escherichia coli	Pure ZnO	Inhibition Method	25 mm	Present work
Staphylococcus aureus	(200 mg/mL)		25 mm	

commercial bacterial strains like *E-coli* and *S.Aureus*, with each sample concentration of 200 mg/mL. The inhibition zone was measured in (mm), and the corresponding inhibition zone for both bacterial strains and different prepared materials is shown in the petri dish in Fig. 18 and Fig. 19. Also, the estimated inhibition in mm for each material and bacterial strains are enclosed in S6. These observations suggest that pure ZnO has a better antibacterial activity for both bacterial strains, and ZnO@C nanocomposite (sample 4) has a better antibacterial activity for *S.Aureus* than *E-coli* bacteria, compared to other prepared materials. A comparative analysis of the antibacterial activity of different photocatalysts is illustrated in Table 4.

4. Conclusion

In this study, we have prepared low-cost and efficient ZnO@C nanocomposite based on the waste scrap tire-derived activated carbon. Four different AC contents, including 2, 4, 6, and 8 mg, were used to develop composites with ZnO via a simple hydrothermal technique. The morphology, crystalline features, optical properties, and antibacterial results exhibited by the nanocomposites gave significant results compared with pristine ZnO. The composite was applied to remove the MG as a pollutant dye. An excellent degradation of 81% and 93.78% of dye was achieved with maximum AC dosage (sample 4) at high and low dye concentrations. Initial dye concentration and solution pH significantly impacted the degradation performance of ZnO@C nanocomposite. The MG degraded 100% at the pH of 12 adjusted in the low concentration of MG. The PL, EIS, and ECSA investigation results exhibited an increase in the surface area and a decrease in charge transfer of the nanocomposites compared to the pure ZnO. An optical examination revealed a significant reduction in the bandgap of the nanocomposite compared to the pure ZnO, endorsing enhanced efficiency. Finally, the antibacterial activity of synthesized nanocomposites was

measured, and as a result, the destruction of commercial bacterial strains was observed. The performance of ZnO@C nanocomposites could be assigned to the synergetic effect between AC and ZnO. Hence, wasted tire scrap could be used to design a new class of carbon materials for potential applications like energy conversion, energy storage, and environmental applications.

Abbreviations

Malachite Green (MG)
Activated Carbon (AC)
Zinc Oxide (ZnO)
Electrochemical Active Surface Area (ECSA)
Electrochemical Impedance Spectroscopy (EIS)
Photo Luminance (PL)
Scanning Electron Microscope (SEM)
X-ray Diffraction (XRD)
Fourier Transform Infrared Spectroscopy (FTIR)
Visible light (VL)
Ultraviolet (UV)
Activated Carbon-Assisted Zinc Oxide (ZnO@C)
Zinc Nitrate Hexahydrate ($H_{12}N_2O_{12}Zn$)
Hexamethylene Tetramine ($(CH_2)_6N_4$)
Potassium Hydroxide (KOH)
Acetone ($(CH_3)_2CO$)
Methanol (CH_3OH)
That is (i-e)
Hydro Chloric Acid (HCl)
Sodium Hydroxide (NaOH)
Silver Nitrate ($AgNO_3$)
Ascorbic Acid ($C_6H_6O_8$)
Ethylenediamine Tetraacetate (EDTA)
Hydroxyl Radicals (•OH)
Oxygen (O_2)
Degree Celsius (°C)
Valence Band (VB)
Conduction Band (CB)
Electron Volt (eV)
Potential of Hydrogen (pH)
Cyclic Voltammetry (CV)
Elements with Constant Phase (CPE1)
Holes (h^+)
Electrons (e^-)
Ethanol (C_2H_5OH)

Authors contributions

Authors were equally contributed in acquisition and analysing the data as well as preparing the paper.

Availability of data and materials

The data that support the findings of this study are available from the corresponding author upon reasonable request.

Conflict of interests

The authors declare that they have no known competing financial interests or personal relationships that could have appeared to influence the work reported in this paper.

References

[1] J. Nyika and D. Megersa. *J. Water Health*, **20**(2022)(2):329–343. DOI: https://doi.org/10.2166/wh.2022.228.

[2] M. Afkhami, B. Zahraie, and M. Ghorbani. *J Arid Environ.*, **199**(2022):104715. DOI: https://doi.org/10.1016/j.jaridenv.2022.104715.

[3] R. Al-Tohamy, S.A. Sameh, L. Fanghua, M. Kamal, Y.A-G. Okasha, T.E. Mahmoud, J. Haixin, F. Yinyi, and S. Jianzhong. *Ecotoxicol. Environ. Saf.*, **231**(2022):113160. DOI: https://doi.org/10.1016/j.ecoenv.2021.113160.

[4] A.A. Shah, M.A. Bhatti, A. Tahira, A.D. Chandio, I.A. Channa, A.G. Sahito, E. Chalangar, M. Willander, O. Nur, and Z.H. Ibupoto. *Ceram. Inter*, **46**(2020)(8):9997–10005, . DOI: https://doi.org/10.1016/j.ceramint.2019.12.024.

[5] Md. K. Hasan, A. Shahriar, and K.U. Jim. *Heliyon*, **5**(2019)(8). DOI: https://doi.org/10.1016/j.heliyon.2019.e02145.

[6] A. Sachidhanandham and A.P. Periyasamy. Environmentally friendly wastewater treatment methods for the textile industry. in handbook of nanomaterials and nanocomposites for energy and environmental applications[m]. *Springer*, (2021:2269–2307. DOI: https://doi.org/10.1007/978-3-030-36268-3-54.

[7] Sh. Samsami, M. Mohamadizaniani, M.H. Sarrafzadeh, E.R. Rene, and M. Firoozbahr. *Process safety and environmental protection*, **143**(2020):138–163. DOI: https://doi.org/10.1016/j.psep.2020.05.034.

[8] M.A. Bhatti, A. Tahira, A.D. Chandio, KH. Faryal Almani, A. Liaquat Bhatti, B. Waryani, A. Nafady, and Z.H. Ibupoto. *Res. Chem. Intermed.*, **47**(2021): 1581–1599, . DOI: https://doi.org/10.1007/s11164-020-04391-6.

[9] M.A. Bhatti, Kh.F. Shah, A.A. andd Almani, A. Tahira, S.E. Chalangar, A.D. Chandio, O. Nur, M. Willander, and Z.H. Ibupoto. *Ceramics Inter*, **45**(2019)(17):23289–23297, . DOI: https://doi.org/10.1016/j.ceramint.2019.08.027.

[10] Z.A. Ujjan, M.A. Bhatti, A.A. Shah, A. Tahira, N.M. Shaikh, SH. Kumar, and Mugheri A.Q. *Ceram. Inter.*, **48**(2022)(4):5535–5545. DOI: https://doi.org/10.1016/j.ceramint.2021.11.098.

[11] A. Chawla, A. Sudhaik, R. Kumar, P. Raizada, A.A. Parwaz Khan, T. Ahamad, V.H. Nguyen, R. Selvasembian, A. Kaushik, and P. Singh. *J. Environ. Chem. Eng.*, **12**(2024)(4):113125. DOI: https://doi.org/10.1016/j.jece.2024.113125.

[12] S. Banerjee, S.C. Pillai, F. Falaras, K.E. O'shea, J.A. Byrne, and D.D. Dionysiou. *J. Physic. Chem. Lett.*, **5**(2014)(15):2543–2554. DOI: https://doi.org/10.1021/jz501030x.

[13] M.A. Bhatti, A. Tahira, A.A. Shah, U. Aftab, B. Vigolo, A.R. Khattab, A. Nafady, I.A. Halepoto, M. Tonezzer, and Z.H. Ibupoto. *RSC Adv.*, **12**(2022)(39):25549–25564, . DOI: https://doi.org/10.1039/D2RA04749G.

[14] M.A. Bhatti, A.A. Shah, Kh.F. Almaani, A. Tahira, A.D. Chandio, M. Willander, and O. Nur. *J. Nanosci. Nanotech.*, **21**(2021)(4):2511–2519, . DOI: https://doi.org/10.1166/jnn.2021.19107.

[15] C. Karthikeyan, P. Arunachalam, K. Ramachandran, A. M. Al-Mayouf, and S.J.J.O.A. Karuppuchamy. *J. Alloy. Comp.*, **828**(2020):154281. DOI: https://doi.org/10.1016/j.jallcom.2020.154281.

[16] V. Soni, P. Singh, S. Thakur, T. Ahamad, V.H. Nguyen, V. Chaudhary, N. Kumar, S. Kaya, C. Mustansar Hussain, and P. Raizada. *J. Taiwan Instit. Chem. Eng.*, **159**(2024):105419. DOI: https://doi.org/10.1016/j.jtice.2024.105419.

[17] H. Derikvandi and A. Nezamzadeh-Ejhieh. *J. Hazard. Mater.*, **321**(2017):629–638. DOI: https://doi.org/10.1016/j.jhazmat.2016.09.056.

[18] Sh. Patial, R. Kumar, A. Sudhaik, S. Thakur, N. Kumar, T. Ahamad, S. Kaya, C. M. Hussain, P. Singh, and P. Raizada. *Chem. Soc. Rev.*, **38**(2009):1598–1607. DOI: https://doi.org/10.1039/B805648J.

[19] S. Sharma, A. Sudhaik, P. Raizada, T. Ahamad, S. Thakur, Q. Van Le, R. Selvasembian, V.H. Nguyen, A. Kumar Mishra, and P. Singh. *J. Environ. Chem. Eng.*, (2024):112984. DOI: https://doi.org/10.1016/j.jece.2024.112984.

[20] S.S. Ghumro, B. Lal, and T. Pirzada. *ACS Omega*, **7**(2022)(5):4333–4341. DOI: https://doi.org/10.1021/acsomega.1c06112.

[21] D. Patila, M.B. Sridharaa, J. Manjannaa, and S. Sabaleb. *Iran. J. Catal.*, **13**(2023)(2):157–167. DOI: https://doi.org/10.30495/ijc.2023.1975703.1985.

[22] M.A. Bhatti, K.F. Almaani, A.A. Shah, A. Tahira, A.D. Chandio, A.Q. Mugheri, A.L. Bhatti, B. Waryani, S.S. Medany, and A.J.J.O.C.S. Nafady. *J. Cluster. Sci.*, (2022):1–12, . DOI: https://doi.org/10.1007/s10876-021-02069-6.

[23] A.A. Shah, A.D. Chandio, and Sheikh. A.A. *J. Nanosci. Nanotech.*, **21**(2021)(4):2483–2494, . DOI: https://doi.org/10.1166/jnn.2021.19315.

[24] Z. Amani-Beni and A. Nezamzadeh-Ejhieh. *Analytica chimica acta*, **1031**(2018):47–59. DOI: https://doi.org/10.1016/j.aca.2018.06.002.

[25] M. Mariana, A.K. HPS, E. Mistar, E.B. Yahya, T. Alfatah, M. Danish, and M.J.J.O.W.P.E. Amayreh. *Appl. Organomet. Chem.*, **43**(2021):102221. DOI: https://doi.org/10.1016/j.aca.2018.06.002.

[26] M.A. Bhatti, Kh.F. Almani, A.A. Shah, A. Tahira, I.A. Chana, U. Aftab, and M.H. Ibupoto. *Nanotechnology*, **34**(2022)(3):035602, . DOI: https://doi.org/10.1088/1361-6528/ac98cc.

[27] A. Sirelkhatim, S. Mahmud, A. Seeni, N.H.M. Kaus, L.C. Ann, S.K.M. Bakhori, H. Hasan, and D. Mohamad. *Nano-Micro Lett.*, **7**(2015):219–242. DOI: https://doi.org/10.1007/S40820-015-0040-X.

[28] N. Padmavathy and R. Vijayaraghavan. *Sci. Tech. Adv. Mater.*, **9**(2008). DOI: https://doi.org/10.1088/1468-6996/9/3/035004.

[29] M. Buşilă, V. Muşat, T. Textor, and B. Mahltig. *Rsc Adv.*, **5**(2015)(28):21562–21571. DOI: https://doi.org/10.1039/C4RA13918F.

[30] A. Aditya, S. Chattopadhyay, D. Jha, H.K. Gautam, S. Maiti, and M. Ganguli. *ACS Appl. Mater. Interfac.*, **10**(2018)(18):15401–15411. DOI: https://doi.org/10.1021/acsami.8b01463.

[31] R. Banyal, P. Raizada, T. Ahamad, S. Kaya, M. M. Maslov, V. Chaudhary, C. M. Hussain, and P. Singh. *J. Physic. Chem. Solids*, (2024):112132. DOI: https://doi.org/10.1016/j.jpcs.2024.112132.

[32] M. Čepin, V. Jovanovski, M. Podlogar, and Z.C. Orel. *J. Mater. Chem. B.*, **3**(2015)(6):1059–1067. DOI: https://doi.org/10.1039/C4TB01300J.

[33] E. Özbaşa, B. Elmaslar, Balçıkb, and H.K. Ozcana. *Desalin Water Treat*, **172**(2019):78–85. DOI: https://doi.org/10.5004/dwt.2019.24493.

[34] N. Muttil, S. Jagadeesan, A. Chanda, M. Duke, and S.K. Singh. *Appl. Sci.*, **13**(2022)(1):257. DOI: https://doi.org/10.3390/app13010257.

[35] Y.B. Chan, M. Aminuzzaman, Md. K. Rahman, Y.F. Win, S. Sultana, Sh. Cheah, and Watanabe A. *Green Processing and Synthesis*, **13**(2024)(1): 20230251. DOI: https://doi.org/10.1515/gps-2023-0251.

[36] V. Selvanathan, M. Aminuzzaman, L.X. Tan, Y.F. Win, E.S.G. Cheah, M.H. Heng, and L.H. Tey. *J. Mater. Res. Tech.*, **20**(2022):2931–2941. DOI: https://doi.org/10.1016/j.jmrt.2022.08.028.

[37] B. Shaikh, M.A. Bhatti, A.A. Shah, A. Tahira, A.K. Shah, A. Usto, and U. Aftab. *Nanomaterials*, **12**(2022)(21):3754. DOI: https://doi.org/10.3390/nano12213754.

[38] S.N.U.Sh. Bukhari, A.A. Shah, M.A. Bhatti, A. Tahira, I.A. Channa, A.K. Shah, and A.D. Chandio. *Nanomaterials*, **12**(2022)(20):3568. DOI: https://doi.org/10.3390/nano12203568.

[39] A. Norouzi, A. Nezamzadeh-Ejhieh, and R. Fazaeli. *Mater. Sci. Semiconduct. Processing*, **122**(2021):105495. DOI: https://doi.org/10.1016/j.mssp.2020.105495.

[40] N. Prasad, S.V.M.M. Hariharan Swaminathan, P. Thangaraj, M.R. Viswanathan, and K. Balasubramanian. *Appl. Physic. A*, **122**(2016):1–12. DOI: https://doi.org/10.1007/s00339-016-0121-9.

[41] M. Kamaraj, N.R. Srinivasan, G. Assefa, A.T. Adugna, and M. Kebede. *Environmental Technology & Innovation*, **17**(2020):100540. DOI: https://doi.org/10.1016/j.eti.2019.100540.

[42] S. Senthilkumaar, K. Rajendran, S. Banerjee, T.K. Chini, and V.J.M.S.I.S.P. Sengodan. *Mater. Sci. Semiconduct. Processing*, **11**(2008)(1):6–12. DOI: https://doi.org/10.1016/j.mssp.2008.04.005.

[43] S. Zandi, P. Kameli, H. Salamati, H. Ahmadvand, and M. Hakimi. *Physica B: Condensed Matter*, **406**(2011)(17):3215–3218. DOI: https://doi.org/10.1016/j.physb.2011.05.026.

[44] I.S. Aminu, M. Gumel, W.A. Ahmad, and A.A. Idris. *Amer. J. Anal. Chem.*, **11**(2020)(01):47. DOI: https://doi.org/10.4236/ajac.2020.111004.

[45] N. Mehrabanpour, A. Nezamzadeh-Ejhieh, Sh. Ghattavi, and A. Ershadi. *Appl. Surf. Sci.*, **614**(2023):156252. DOI: https://doi.org/10.1016/j.apsusc.2022.156252.

[46] S.W. Zhao, H.F. Zuo, Y.R. Guo, and Q.J. Pan. *J. Alloy. Comp.*, **695**(2017):1029–1037. DOI: https://doi.org/10.1016/j.jallcom.2016.10.226.

[47] C.T. Lee. *Materials*, **3**(2010)(4):2218–2259. DOI: https://doi.org/10.3390/ma3042218.

[48] A. Yousefi and A. Nezamzadeh-Ejhieh. *Iran. J. Catal.*, **11**(2021)(3):247–259. URL https://journals.iau.ir/article-684355-ba281a758a9084e2a3f2d3bf091152da.pdf.

[49] M. Rezaei and A. Nezamzadeh-Ejhieha. *Inter. J. Hyd. Ener.*, **45**(2020)(46):24749–24764. DOI: https://doi.org/10.1016/j.ijhydene.2020.06.258.

[50] H.P. Jing, C.C. Wang, Y.W. Zhang, P. Wang, and R. Li. *Rsc Adv.*, **4**(2014)(97):54454–54462. DOI: https://doi.org/10.1039/C4RA08820D.

[51] Md. Molla, A. Islam, I. Tateishi, M. Furukawa, H. Katsumata, T. Suzuki, and S. Kaneco. *Open J. Inorg. Non-metal. Mater.*, **7**(2017)(1):1–7. DOI: https://doi.org/10.4236/ojinm.2017.71001.

[52] M. Ramamoorthy, S. Ragupathy, D. Sakthi, V. Arun, and N. Kannadasan. *Results in Materials*, **8**(2020):100144. DOI: https://doi.org/10.1016/j.rinma.2020.100144.

[53] K.V. Karthik, Raghu A.V., K.R. Reddy, R. Ravishankar, M. Sangeeta, N.P. Shetti, and Ch.V. Reddy. *Chemosphere*, **287**(2022):132081. DOI: https://doi.org/10.1016/j.chemosphere.2021.132081.

[54] T. Yang, J. Peng, Y. Zheng, X. He, Y. Hou, L. Wu, and X. Fu. *Appl. Catal. B: Environ.*, **221**(2018):223–234. DOI: https://doi.org/10.1016/j.apcatb.2017.09.025.

[55] M. Rezaei, A. Nezamzadeh-Ejhieh, and A.R. Massah. *Ecotoxic. Environ. Saf.*, **269**(2024):115927, . DOI: https://doi.org/10.1016/j.ecoenv.2024.115927.

[56] S. Meena, D. Vaya, and B.K. Das. *Bullet. Mater. Sci.*, **39**(2016):1735–1743, . DOI: https://doi.org/10.1007/s12034-016-1318-4.

[57] M. Aminuzzaman, P.S. Ng, W.Sh. Goh, S. Ogawa, and A. Watanabe. *Inorg. Nano-Metal Chem.*, **49**(2019)(11):401–411, . DOI: https://doi.org/10.1080/24701556.2019.1661464.

[58] M. Rezaei, A. Nezamzadeh-Ejhieh, and A.R. Massah. *Energy & Fuels*, **38**(2024)(9):7637–7664, . DOI: https://doi.org/10.1021/acs.energyfuels.4c00325.

[59] M. Aminuzzaman, W. Sh. Ying, L.P. ND Goh, and A. Watanabe. *Bullet. Mater. Sci.*, **41**(2018):1–10, . DOI: https://doi.org/10.1007/s12034-018-1568-4.

[60] M. Arunkumar, A.S. Nesaraj, C.E.F. Christy, and Ch.J. Kennady. *Nanotech. Environ. Eng.*, **8**(2023)(3):643–654. DOI: https://doi.org/10.1007/s41204-022-00300-x.

[61] N. Babajani and S. Jamshidi. *J. Alloy. Comp.*, **782**(2019):533–544. DOI: https://doi.org/10.1016/j.jallcom.2018.12.164.

[62] P.L. Meena, K. Poswal, and A.K. Surela. *Water Environ. J.*, **36**(2022)(3):513–524, . DOI: https://doi.org/10.1111/wej.12783.

[63] A.M. Saad, R. Abukhadra, S.A.K. Ahmed, A.M. Elzanaty, A.H. Mady, M.A. Betiha, J.J. Shim, and A.M. Rabie. *J. Environ. Manag.*, **258**(2020):110043. DOI: https://doi.org/10.1016/j.jenvman.2019.110043.

[64] D.R. Rout, Sh. Chaurasia, and H.M. Jena. *J. Environ. Manag.*, **318**(2022):115449. DOI: https://doi.org/10.1016/j.jenvman.2022.115449.

[65] R. Yadav, T.S. Chundawat, P. Rawat, G.K. Rao, and D. Vaya. *Bullet. Mater. Sci.*, **44**(2021):1–8. DOI: https://doi.org/10.1007/s12034-021-02533-z.

[66] W.W. Loo, W.L. Pang, S. Lim, K.H. Wong, Ch.W. Lai, and A.Z. Abdullah. *Chemosphere*, **272**(2021):129588. DOI: https://doi.org/10.1016/j.chemosphere.2021.129588.

[67] S. Sukri, E. Isa, and K. Shameli. Photocatalytic degradation of malachite green dye by plant-mediated biosynthesized zinc oxide nanoparticles, in: Iop conference series: materials science and engineering. *IOP Publishing*, (2020):012034. DOI: https://doi.org/10.1088/1757-899X/808/1/012034.

[68] N. Tiwari, S. Chakrabortty, K. Samal, S. Moulick, B.G. Mohapatra, S. Samanta, P.K. Mohapatra, et al. *J. Taiwan Instit. Chem. Eng.*, **145**(2023):104800. DOI: https://doi.org/10.1016/j.jtice.2023.104800.

[69] Y. Yulizar, I. Abdullah, R.M. Surya, and N.L. Alifa. *J. Environ. Manag.*, **342**(2023):118139. DOI: https://doi.org/10.1016/j.jenvman.2023.118139.

[70] Y. Zhang, B. Liu, N. Chen, Y. Du, T. Ding, Y. Li, and W. Chang. *Optical Materials*, **133**(2022):112978. DOI: https://doi.org/10.1016/j.optmat.2022.112978.

[71] R. Madhushree, J. R. Jaleel Uc, D. Pinheiro, N. K. Renuka, S. Devi Kr, J. Park, S. Manickam, and M.Y. Choi. *Environ. Res.*, **214**(2022):113742. DOI: https://doi.org/10.1016/j.envres.2022.113742.

[72] Sh. Wang, Zh. Chen, Y. Zhao, Ch. Sun, and J. Li. *J. Rare Earths*, **39**(2021)(7):772–780, . DOI: https://doi.org/10.1016/j.jre.2020.04.009.

[73] R. Ebrahimi, Kh. Hossienzadeh, A. Maleki, R. Ghanbari, R. Rezaee, M. Safari, and B. Shahmoradi. *J. Environ. Health Sci. Eng.*, **17**(2019):479–492. DOI: https://doi.org/10.1007/s40201-019-00366-x.

[74] N. Van Hung, B.T.M. Nguyet, B.T.T. Linh, N.H. Nghi, N.T. Tuoi, and N.A. Tien. *Vietnam J. Catal. Adsorp*, **9**(2020)(3):1–8. DOI: https://doi.org/10.51316/jca.2020.041.

[75] A.A. Menazea and N.S. Awwad. *J. Mater. Res. Tech.*, **9**(2020)(4):9434–9441. DOI: https://doi.org/10.1016/j.jmrt.2020.05.103.

[76] Y. Wang, X. Xue, and H. Yang. *Vacuum*, **101**(2014):193–199, . DOI: https://doi.org/10.1016/j.vacuum.2013.08.006.

[77] K. Kaviyarasu, N. Geetha, K. Kanimozhi, C. Maria Magdalane, S. Sivaranjani, A. Ayeshamariam, J. Kennedy, and M. Maaza. *Mater. Sci. Eng. C*, **34**(2021):325–333. DOI: https://doi.org/10.1016/j.msec.2016.12.024.

[78] S. Albukhaty, L. Al-Bayati, H. Al-Karagoly, and S. Al-Musawi. *Animal Biotech*, **33**(2022)(5):864–870. DOI: https://doi.org/10.1080/10495398.2020.1842751.

[79] V.T. Nguyen, V.T. Vu, T.H. Nguyen, T.A. Nguyen, V.Kh. Tran, and P. Nguyen-Tri. *J. Comp. Sci.*, **3**(2019)(2):61. DOI: https://doi.org/10.3390/jcs3020061.

[80] A. Taha, M.B. Aissa, and E. Da'na. *Molecules*, **25**(2020)(7):1586. DOI: https://doi.org/10.3390/molecules25071586.